Step engineering for nucleation and domain orientation control in WSe$_2$ epitaxy on c-plane sapphire

Haoyue Zhu
  The Pennsylvania State University

Nadire nayir
  Karamanoglu Mehmetbey University/The Pennsylvania State University

Tanushree Choudhury
  Indian Institute of Technology Bombay/The Pennsylvania State University

Anushka Bansal
  The Pennsylvania State University

Benjamin Huet
  The Pennsylvania State University

Kunyan Zhang
  The Pennsylvania State University

Alexander Puretzky
  Oak Ridge National Laboratory

Saiphaneendra Bachu
  The Pennsylvania State University

Krystal York
  Western Michigan University

Thomas Mc Knight
  The Pennsylvania State University

Nicholas Trainor
  Pennsylvania State University

Ke Wang
  Pennsylvania State University

Robert Makin
  Western Michigan University

Steven Durbin
  Western Michigan University

Shengxi Huang
  The Pennsylvania State University/Rice University

Nasim Alem

Pennsylvania State University

Vincent Crespi
Pennsylvania State University   https://orcid.org/0000-0003-3846-3193

Adri Van Duin
Pennsylvania State University   https://orcid.org/0000-0002-3478-4945

Joan Redwing (✉ jmr31@psu.edu)
The Pennsylvania State University   https://orcid.org/0000-0002-7906-452X

Article

Keywords:

Abstract

Epitaxial growth of 2D transition metal dichalcogenides (TMDs) on sapphire has emerged as a promising route to wafer-scale single crystal films. Steps on the sapphire act as sites for TMD nucleation and can impart a preferred domain orientation resulting in a significant reduction in mirror twins. Here we demonstrate control of both the nucleation site and unidirectional growth direction of WSe_2 on c-plane sapphire by metalorganic chemical vapor deposition (MOCVD). The unidirectional orientation is found to be intimately tied to growth conditions via changes in the sapphire surface chemistry which control the step edge location of WSe_2 nucleation imparting either a 0° or 60° orientation relative to the underlying sapphire lattice. The results provide insight into the role of surface chemistry on TMD nucleation and domain alignment and demonstrate the ability to engineer domain orientation over wafer-scale substrates.

Full Text

Two-dimensional (2D) transition metal dichalcogenides (TMDs) with desired properties are ideal candidates for novel applications, such as 3D integrated devices on Si complementary metal−oxide−semiconductor (CMOS), sensors, and optoelectronics.[1,2,3,4] In addition to the intensively studied MoS_2, monolayer WSe_2, a direct bandgap semiconductor with an optical gap of ∼1.65 eV, also shows attractive properties.[5,6] WSe_2 is distinguished from other TMDs by its enhanced spin-orbit coupling and large splitting of the valence band maximum (0.46 eV for WSe_2, as compared to 0.15 eV for MoS_2), making it a promising material for spintronics.[7,8] The ambipolar characteristics of WSe_2 also enable p-type behavior compared to the commonly observed n-type doping in WS_2 and MoS_2.[9,10,11,12]

Due to the small size of mechanically exfoliated flakes from bulk crystals, research has focused on epitaxial growth of TMDs as a pathway to wafer-scale single crystal monolayers and few-layer films.[13,14] C-plane sapphire ((0001) a-Al_2O_3) has emerged as a promising substrate for epitaxial growth due to its crystallographic compatibility, chemical and thermal stability under typical growth environments, and commercial availability in wafer diameters up to 8 inches. Epitaxial growth of WSe_2 on c-plane a-Al_2O_3 has been demonstrated[15,16] where growth on a 1x1 Al-terminated (0001) sapphire surface, exhibits commensurability via a 3-on-2 superstructure (a_{WSe2}=3.30 Å and $a_{a\text{-}Al2O3}$=4.76Å) with the WSe_2 aligned in the same crystallographic direction as the a-Al_2O_3 (Figs. 1a and S1).[17] The non-centrosymmetric C_{3v} lattice of TMDs leads to the equivalency of anti-parallel domains with lattice rotation angles of 0° and 60° (Fig. 1a) or ± 30° relative to the <110> axis.[18] The merging of domains with 60° in-plane rotation leads to the formation of inversion domain boundaries (IDBs), also referred to as mirror twin grain boundaries (MTBs).[19,20] IDBs have been demonstrated to exhibit metallic character and can act as conducting channels within the semiconducting monolayer that negatively impact both electrical and optical properties.[21,22,23]

Steps on the *c*-plane sapphire surface play an important role in TMD nucleation and orientation. On-axis *c*-plane sapphire substrates typically have a small miscut angle of ~0.2° toward the m-axis (<100>) which produces steps that are aligned roughly parallel to the a-axis (<110>) (Fig. S2). Chen *et al.* demonstrated that the steps act as preferred sites for WSe_2 nucleation and impart directionality to the growing domains.[24] Similar unidirectional domains have been reported for epitaxial growth of WS_2[25] and MoS_2[26] on c-plane sapphire miscut ~0.2° toward the m-axis and a-axis, respectively. However, the presence of steps alone is not sufficient to achieve unidirectional domains. For example, Hwang *et al.*[27] observed step-edge aligned nucleation of $MoSe_2$ on *c*-plane sapphire only when H_2 was added to the Ar carrier gas and Sunega *et al.*[28] reported epitaxial growth of MoS_2 with +30°/-30° or 0°/60° lattice rotation angles only under increased sulfur flux. Consequently, both the presence of steps and the growth chemistry play a role in TMD nucleation and alignment, but chemistry effects are not as well understood.

In this study, we demonstrate that steps on sapphire act as sites for WSe_2 nucleation and furthermore that the preferred site for WSe_2 nucleation on the step edge can be switched from the top to the bottom edge of the step by varying growth conditions, resulting in a change in the preferred domain orientation from 0° to 60°, respectively. Our combined experimental and theoretical results provide insight into the role of surface step structure and chemistry on TMD nucleation and domain alignment that can be exploited to reproducibly achieve wafer-scale single crystal monolayers.

 WSe_2 monolayer films were grown by metalorganic vapor phase epitaxy (MOCVD) on 2" diameter c-plane sapphire substrates using a modified three-step process (nucleation, ripening, lateral growth)[15] with $W(CO)_6$ and H_2Se as precursors in a H_2 carrier gas (see Methods and Figure S3). Using a lateral growth time of 10 min and reactor pressure of 200 Torr, isolated WSe_2 domains are present on the substrate, which enables a determination of their orientation relative to the underlying sapphire (Fig. 1b,c). The majority of the WSe_2 domains point in opposite directions relative to the m-axis of the sapphire; along the and which are designated as 0° and 60° domains, respectively (Fig. 1a). Statistical analysis indicates that ~87% of the domains (excluding partially coalesced domains) exhibit a 0° orientation while the remainder are 60° oriented (Fig. 1c). The preferred orientation is uniformly observed across the entire 2" substrate excluding the edge region (Fig. S4). In-plane X-ray diffraction (XRD) f-scans of the {110} planes of WSe_2 and a-Al_2O_3 show six-fold rotational symmetry and demonstrate that the WSe_2 grows epitaxially on the substrate with the epitaxial relationship of $[110]WSe_{2(0001)}$ // $[110]a\text{-}Al_2O_{3(0001)}$. (Fig. 1d).

The effect of growth temperature on WSe_2 domain orientation was probed by varying the lateral growth temperature from 650 °C to 1000 °C while holding all other growth conditions constant (see Methods and Fig. S3). Again, in-plane XRD f-scans show an epitaxial relationship of $[110]WSe_{2(0001)}$//$[110]a\text{-}Al_2O_{3(0001)}$ for growth temperatures from 750 °C to 1000 °C (Fig. 1e). The full-width-at-half-maximum (FWHM) of the f-scan peak of WSe_2, which is a measure of the in-plane rotational misorientation of domains,[29] decreases from 0.47° at 750 °C to 0.16° at 1000 °C indicating an improvement in the epitaxial registry at higher growth temperatures (Fig. 1f). In addition, the percentage of 0° domains increases from

~60% for the WSe$_2$ sample grown at 650- 750 °C to ~85% for the WSe$_2$ grown at 1000 °C (Figs. 1g-i and S5). The surface coverage of the WSe$_2$ domains decreases from 37% at 650 °C to 20% at 1000 °C likely due to reduced adsorption of precursors on the substrate at elevated temperatures.

To investigate the origin of the preferred orientation, the W(CO)$_6$ precursor flux was reduced and the growth was terminated after the nucleation and ripening steps. A significant fraction of the WSe$_2$ nuclei (white dots) are localized at the top edge of the steps, as highlighted by the white arrows (Fig. 2a), the histogram and schematic illustration (Fig. 2b). After lateral growth of 5 min, the nuclei grow into triangular domains (Fig. 2c). As shown in the histogram and schematic (Fig. 2d), the domains near the terrace centers show both the 0° (orange) and 60° (blue) orientations, present in similar fractions. However, the domains that nucleate at the top edge of the step (red) and grow across the terrace are much more frequently observed than those which initiate at the bottom step edge (light blue).

The role of steps as nucleation sites is well established in traditional epitaxy and has been reported previously for TMD growth on c-plane sapphire.[24,27] The side edge facet of the step is typically the thermodynamically preferred site for nucleation due to the preponderance of dangling bonds, which results in growth from the bottom edge of the step. Our observations, however, find that the nuclei are localized at the top edge of the steps with their zig-zag edge roughly aligned to the step edge and grow across the terrace rather than over the step edge giving rise to the observed 0orientation. However, the WSe$_2$ orientation is not solely determined by the step direction, which can vary by several degrees from substrate to substrate. Figures 3a-b show two examples where the step direction varies by as much as ± 10°-12° from the A<1120> axis. The WSe$_2$ domains do not align to the steps, rather they retain the [110]WSe$_{2(0001)}$//[110]a-Al$_2$O$_{3(0001)}$ epitaxial relationship (Fig. 3c-d). This can be explained by assuming that at the early stage of growth, when WSe$_2$ nuclei have not yet obtained their equilibrium zig-zag structure, the nuclei have slanted edges with kinks which interact strongly with the step edges (see SI and Figure S6). The slanted edges disappear quickly during kink flow growth of the edge leading to completion of the linear zig-zag edge which is aligned parallel to the A<1120> axis rather than the step edge. Thus, while the steps act as sites for nucleation and impart directionality, the WSe$_2$ domains remain oriented to the underlying c-plane sapphire lattice regardless of the exact step angle.

Density functional theory (DFT) calculations were carried out to explore the epitaxial relationship between WSe$_2$ and a flat c-plane sapphire to assess the role of the steps. Thermal annealing of c-plane sapphire in H$_2$ at high temperatures (~900ºC) is known to alter the sapphire surface resulting in a loss of -OH groups leaving an Al-terminated surface.[30] Given the high temperature (850-1000 °C), H$_2$-rich growth environment, the c-plane sapphire surface is assumed to be 1´1 Al-terminated, akin to previous reports.[14] Direct epitaxy of WSe$_2$ on Al-terminated sapphire would destroy the van der Waals nature of the interface (Fig. S7a). Therefore, the Al-terminated surface is assumed to react readily with H$_2$Se, which is present in excess in the growth ambient, resulting in a Se-passivated surface. The WSe$_2$ then interacts with the Se-

passivated sapphire surface via quasi van der Waals epitaxy which is consistent with the interface structure as assessed by transmission electron microscopy (Figs. S7b,c and S8).

The relative total energy of different orientations of WSe_2 on Se-passivated c-plane sapphire was then computed by rotating a WSe_2 cluster with a dimension of 13.16 Å with respect to the [10$\bar{1}$0] direction of sapphire where $0° \rightarrow$ [10$\bar{1}$0]$WSe_{2\ (0001)}$//[10$\bar{1}$0]$Al_2O_{3\ (0001)}$ and $30° \rightarrow$ [10$\bar{1}$0]$WSe_{2\ (0001)}$//[11$\bar{2}$0]$Al_2O_{3\ (0001)}$ (Fig. S9). On flat Se-passivated sapphire, the 30° orientation of WSe_2 was found to be a more stable configuration (Fig. 3f). However, as shown in Figs. 1-3 and other reports,[15,17] the 0°/60° orientations are observed experimentally. This indicates that the presence of step edges along the A<1120> axis, which act as sites for WSe_2 nucleation, induce the 0/60° alignment (Fig. 3e-f) instead of the predicted 30° alignment (Fig. 3f-g). The presence of A<1120> steps reduces symmetry by external perturbation (e.g., high adsorption sites on step edges) and by consequence, removes the degeneracy in the formation energy of WSe_2 on sapphire (Fig. 3f); in other words, the 30° option disappears at the step edges, stabilizing the 0° (or 60°) alignment (Fig. 3e).

To further investigate the effect of growth conditions on WSe_2 domain orientation, additional growths were carried out using the modified three-step process with 1000°C lateral growth temperature, but the reactor pressure was increased from 200 Torr to 700 Torr to increase the partial pressure of both H_2 and H_2Se within the growth environment. As previously discussed, at 200 Torr, the majority of the WSe_2 domains exhibit the 0° orientation (Fig. 4a), however, at 700 Torr, the predominant domain direction switches to 60° (Fig. 4b). The 60° orientation observed at 700 Torr indicates that the WSe_2 domains are now nucleating at the bottom edge of the steps, similar to previous reports for step-directed TMD growth.[24,27]

DFT calculations were used to identify the thermodynamically preferred site for WSe_2 nucleation on the steps for comparison to the experimental results (Figs. S10-15). The existence of an oxygen remnant on the bottom terrace next to the step edge due to incomplete removal of -OH from the sapphire surface leads to WSe_2 growth on the top step edge rather than the bottom (Figs. 4c-e and S11-13). WSe_2 that nucleates at the top edge remains there (Fig. S10, S12-15 and Movies S2 and S6) while WSe_2 that initially nucleates at the bottom edge moves from the bottom to top (Fig. S10-15 and Movies S1 and S5). The existence of an O-remnant induces first the reconstruction of the step edge, followed by the movement of WSe_2 from the bottom to the top terrace during the relaxation (Fig. 4e) consistent with the experimental results obtained at 200 Torr (Fig. 4a). However, for sapphire that is fully Al-terminated and passivated with Se with no O-remnant (Figs. 4d and S14-15 and Movies S3, S4, S7, S8), WSe_2 remains on the bottom of the step edge (Fig. S14f) during relaxation which is thermodynamically more stable than the top edge (Fig. S14e) with an energy difference of 0.13 eV consistent with the result obtained at 700 Torr (Fig. 4b).

 DFT calculations reveal that in the presence of steps, the extent of Al termination of the sapphire surface will be dependent on the growth conditions (Figs. S16-S17). As the sapphire substrate with −OH termination is heated in hydrogen, the surface releases H_2O but this does not occur uniformly. Oxygen

dissociation from the top terrace is energetically more favorable (1.24 eV) than that from the middle (1.28 eV) and bottom terraces (1.73 eV) (Fig. S17). The H_2O loss occurs at the top of the steps and the terrace regions first and the bottom of the steps last (Figs. S16). At lower reactor pressures, the chemical potential of hydrogen is reduced, and consequently, O-remnants can still be present at the bottom of the steps. In this case, it is thermodynamically more likely for the WSe_2 to nucleate at the top step edge as observed experimentally at 200 Torr (Fig. 4a). The results demonstrate that the preferential alignment of WSe_2 domains is dependent not only on the presence of steps but also on the surface termination of the sapphire substrate and the structure and chemistry of the step edges (Figure S10-17).

The impact of unidirectional alignment on the structural and optical properties of coalesced WSe_2 monolayers was assessed for films grown at a reactor pressure of 200 Torr and lateral growth temperature of 1000 °C, which provided the highest percentage of 0° oriented domains. As the lateral growth time is increased from 2 min to 26 mins, the triangular WSe_2 domains grow laterally and begin to merge (Figs 5a and S18). At 22 mins of lateral growth, the void regions that remain between coalesced WSe_2 domains also have triangular shapes opposite to that of the 0° domains providing additional evidence for the unidirectional nature of the monolayer. Over this time window, the surface coverage of WSe_2 increases approximately linearly with lateral growth time (Fig. 5b). At 26 mins, the WSe_2 monolayer is nearly fully coalesced across the central portion of the 2" wafer (Fig. S19) and the surface contains undulations arising from the steps on the underlying sapphire. In-plane XRD of this sample confirms that it has retained the $[110]WSe_{2(0001)}$ // $[110]a\text{-}Al_2O_{3(0001)}$ epitaxial alignment (Fig. 5c) and the FWHM of the f-scan peak of WSe_2 has further narrowed to 0.14° (Fig. 5d).

Raman spectroscopy and photoluminescence (PL) measurements were carried out at room temperature (RT) on a WSe_2 monolayer that was grown for 30 mins lateral growth time to ensure complete film coalescence. The WSe_2 was removed from the sapphire and transferred to a SiO_2/Si substrate (see Methods and Fig. S20a-d). The RT Raman spectrum (Fig. S20e) shows the characteristic E_{2g}^1, A_{1g} and $2LA$ modes associated with single-layer 2H-WSe_2. The RT PL spectrum (Fig. S20f) shows a strong peak that can be deconvoluted into a neutral exciton peak and a negatively charged exciton (trion) peak located at ~1.68 eV and ~1.65 eV, respectively. There is negligible change in Raman and PL peak positions and FWHM as a function of position across the transferred WSe_2 (Figs. S20g-h) which suggests uniform properties across the wafer-scale film.

Second harmonic generation (SHG) and dark-field transmission electron microscopy (DFTEM) were used to assess the microstructure and orientation of the coalesced WSe_2 monolayer. Figure 6(a) shows a typical SHG map of the WSe_2 monolayer on c-plane sapphire. The map reveals ~ 2-4 mm sized monolayer regions decorated with bilayers in 3R (red spots) and 2H (blue spots) stacking configurations, which typically are 1mm in size (see SI for details). The polarization-resolved SHG measurements confirm that the monolayer regions have the same crystal orientation (see Methods and Figs. S21-22). For DFTEM, the WSe_2 monolayer sample was transferred from the sapphire to a Quantifoil holey carbon Cu

TEM grid (see Methods). The composite DFTEM image shown in Figure 6b was formed by stitching a 5´5 array of individual DFTEM images[25,31,32] (see the Methods and Fig. S23). The composite DFTEM image reveals the presence of triangular shaped 60° oriented domains outlined by trapezoidal holes (yellow circles). The trapezoidal holes define the boundaries between 0° and 60° domains (Fig. S23b-d) and were IDBs or MTBs that were preferentially etched away by the NaOH solution during the transfer process. The 60° domains account for <10% of the 25 μm^2 viewing area (Fig. 6b) which is consistent with the areal coverage of 60° domains measured by AFM prior to coalescence (Fig. 1g). Bilayer islands (bright triangles) and voids (small dark triangles) are also present which formed during layer transfer or from incomplete film coalescence.

The high optical quality of the WSe_2 is confirmed by variable temperature PL. WSe_2 transferred onto SiO_2/Si exhibits two peaks in the PL spectrum at 77 K under 532 nm excitation (Figure S24). The PL emission at 1.730 eV is identified as the A exciton, while the peak at 1.695eV is attributed to the negatively charged exciton (trion). Polarization-resolved PL (Figure S25) was measured under a left-handed circularly polarized (σ_-) laser. The circular helicity is defined as P = $(I_- - I_+)/(I_- + I_+)$, in which I_- and I_+ are the intensity of the σ_- and σ_+ components of the PL signal, respectively. The σ_- and σ_+ components correspond to the exciton transition at K and K' valleys, respectively, as determined by the valley-selective optical selection rules.[33,34] The circular helicity of the exciton (trion) is 0.28 (0.16) at 77 K as shown in Figure 6(c), which are comparable to that reported from an exfoliated WSe_2 monolayer flake at the same temperature.[35] The circular helicity of trion and exciton both drop as a function of increasing temperature (Fig. 6(d)), which is explained by a higher intervalley scattering rate due to the increased phonon population at high temperatures consistent with exfoliated WSe_2 monolayers.[33,36] The observed circular helicity indicates a high level of valley coherence, consistent with a low fraction of IDBs, demonstrating the high quality of the coalesced WSe_2 monolayer.[37]

Declarations

Acknowledgements

Author Contributions

Competing financial interests

References

1   Acerce, M.; Voiry, D.; Chhowalla, M. Metallic 1T Phase MoS2 Nanosheets as Supercapacitor Electrode Materials. Nat. Nanotechnol. 2015, 10 (4), 313–318. https://doi.org/10.1038/nnano.2015.40.

2   Late, D. J.; Doneux, T.; Bougouma, M. Single-Layer MoSe2 Based NH3 Gas Sensor. Appl. Phys. Lett. 2014, 105 (23), 3–7. https://doi.org/10.1063/1.4903358.

3   Tan, H.; Fan, Y.; Zhou, Y.; Chen, Q.; Xu, W.; Warner, J. H. Ultrathin 2D Photodetectors Utilizing Chemical Vapor Deposition Grown WS2with Graphene Electrodes. ACS Nano 2016, 10 (8), 7866–7873. https://doi.org/10.1021/acsnano.6b03722.

4   Akinwande, D.; Huyghebaert, C.; Wang, C. H.; Serna, M. I.; Goossens, S.; Li, L. J.; Wong, H. S. P.; Koppens, F. H. L. Graphene and Two-Dimensional Materials for Silicon Technology. Nature 2019, 573 (7775), 507–518. https://doi.org/10.1038/s41586-019-1573-9.

5   Zhou, H.; Wang, C.; Shaw, J. C.; Cheng, R.; Chen, Y.; Huang, X.; Liu, Y.; Weiss, N. O.; Lin, Z.; Huang, Y.; Duan, X. Large Area Growth and Electrical Properties of P-Type WSe2 Atomic Layers. Nano Letters. 2015, 15 (1), 709–713. https://doi.org/10.1021/nl504256y.

6   Terrones, H.; López-Urías, F.; Terrones, M. Novel Hetero-Layered Materials with Tunable Direct Band Gaps by Sandwiching Different Metal Disulfides and Diselenides. Sci. Rep. 2013, 3, 1–8. https://doi.org/10.1038/srep01549.

7   Yuan, H.; Bahramy, M. S.; Morimoto, K.; Wu, S.; Nomura, K.; Yang, B. J.; Shimotani, H.; Suzuki, R.; Toh, M.; Kloc, C.; Xu, X.; Arita, R.; Nagaosa, N.; Iwasa, Y. Zeeman-Type Spin Splitting Controlled by an Electric Field. Nat. Phys. 2013, 9 (9), 563–569. https://doi.org/10.1038/nphys2691.

8   Xiao, D.; Liu, G. Bin; Feng, W.; Xu, X.; Yao, W. Coupled Spin and Valley Physics in Monolayers of MoS 2 and Other Group-VI Dichalcogenides. Phys. Rev. Lett. 2012, 108 (19), 1–5. https://doi.org/10.1103/PhysRevLett.108.196802.

9   Fang, H.; Chuang, S.; Chang, T. C.; Takei, K.; Takahashi, T.; Javey, A. High-Performance Single Layered WSe2 p-FETs with Chemically Doped Contacts. Nano Lett. 2012, 12 (7), 3788–3792. https://doi.org/10.1021/nl301702r.

10   Radisavljevic, B.; Radenovic, A.; Brivio, J.; Giacometti, V.; Kis, A. Single-Layer MoS2 Transistors. Nat. Nanotechnol. 2011, 6 (3), 147–150. https://doi.org/10.1038/nnano.2010.279.

11   Iqbal, M. W.; Iqbal, M. Z.; Khan, M. F.; Shehzad, M. A.; Seo, Y.; Park, J. H.; Hwang, C.; Eom, J. High-Mobility and Air-Stable Single-Layer WS2 Field-Effect Transistors Sandwiched between Chemical Vapor Deposition-Grown Hexagonal BN Films. Sci. Rep. 2015, 5 (April), 1–9. https://doi.org/10.1038/srep10699.

12   Chuang, H. J.; Tan, X.; Ghimire, N. J.; Perera, M. M.; Chamlagain, B.; Cheng, M. M. C.; Yan, J.; Mandrus, D.; Tománek, D.; Zhou, Z., High Mobility WSe2 p - And n - Field-Effect Transistors Contacted by Highly Doped Graphene for Low-Resistance Contacts. Nano Lett. 2014, 14 (6), 3594–3601. https://doi.org/10.1021/nl501275p.

13   Choudhury, T.H., Zhang, X., Al Balushi, Z.Y., Chubarov, M., Redwing, J.M., Epitaxial growth of two-dimensional layered transition metal dichalcogenides, Ann. Rev. Mater. Res. 2020, 50, 155-177. https://doi.org/10.1146/annurev-matsci-090519-113456.

14   Mortelmans, W., De Gendt, S. Heyns, M., Merckling C., Epitaxy of 2D chalcogenides: Aspects and consequences of weak van der Waals coupling, Appl. Mater. Today 2021, 22, 100975. https://doi.org/10.1016/j.apmt.2021.100975.

15   Zhang, X.; Choudhury, T. H.; Chubarov, M.; Xiang, Y.; Jariwala, B.; Zhang, F.; Alem, N.; Wang, G. C.; Robinson, J. A.; Redwing, J. M. Diffusion-Controlled Epitaxy of Large Area Coalesced WSe2 Monolayers on Sapphire. Nano Lett. 2018, 18 (2), 1049–1056. https://doi.org/10.1021/acs.nanolett.7b04521.

16   Lin, Y. C.; Jariwala, B.; Bersch, B. M.; Xu, K.; Nie, Y.; Wang, B.; Eichfeld, S. M.; Zhang, X.; Choudhury, T. H.; Pan, Y.; Addou, R.; Smyth, C. M.; Li, J.; Zhang, K.; Haque, M. A.; Fölsch, S.; Feenstra, R. M.; Wallace, R. M.; Cho, K.; Fullerton-Shirey, S. K.; Redwing, J. M.; Robinson, J. A. Realizing Large-Scale, Electronic-Grade Two-Dimensional Semiconductors. ACS Nano 2018, 12 (2), 965–975. https://doi.org/10.1021/acsnano.7b07059.

17   Mortelmans,W., El Kazzi, S., Mehta, A. N., Vanhaeren, D., Conard, T., Meersschaut, J., Nuytten, T., De Gendt, S., Heyns, M., Merckling, C., "Peculiar alignment and strain of 2D WSe2 grown by van der Waals epitaxy on reconstructed sapphire surfaces," Nanotechnology 2019, 30, 465601. https://doi.org/10.1088/1361-6528/ab3c9b.

18   Dong, J., Zhang, L., Dai, X., Ding, F., "The epitaxy of 2D materials growth," Nature Commun. 2020, 11, 5862. https://doi.org/10.1038/s41467-020-19752-3.

19   Zhou, W.; Zou, X.; Najmaei, S.; Liu, Z.; Shi, Y.; Kong, J.; Lou, J.; Ajayan, P. M.; Yakobson, B. I.; Idrobo, J. C. Intrinsic Structural Defects in Monolayer Molybdenum Disulfide. Nano Lett. 2013, 13 (6), 2615–2622. https://doi.org/10.1021/nl4007479.

20   Liu, H.; Jiao, L.; Yang, F.; Cai, Y.; Wu, X.; Ho, W.; Gao, C.; Jia, J.; Wang, N.; Fan, H.; Yao, W.; Xie, M. Dense Network of One-Dimensional Midgap Metallic Modes in Monolayer MoSe2 and Their Spatial Undulations. Phys. Rev. Lett. 2014, 113 (6), 1–5. https://doi.org/10.1103/PhysRevLett.113.066105.

21   Zou, X.; Liu, Y.; Yakobson, B. I. Predicting Dislocations and Grain Boundaries in Two-Dimensional Metal-Disulfides from the First Principles. Nano Lett. 2013, 13 (1), 253–258. https://doi.org/10.1021/nl3040042.

22   Du, L.; Yu, H.; Xie, L.; Wu, S.; Wang, S.; Lu, X.; Liao, M.; Meng, J.; Zhao, J.; Zhang, J.; Zhu, J.; Chen, P.; Wang, G.; Yang, R.; Shi, D.; Zhang, G. The Effect of Twin Grain Boundary Tuned by Temperature on the Electrical Transport Properties of Monolayer MoS2. Crystals 2016, 6 (9), 1–9. https://doi.org/10.3390/cryst6090115.

23   Zhou, S.; Wang, S.; Shi, Z.; Sawada, H.; Kirkland, A. I.; Li, J.; Warner, J. H. Atomically Sharp Interlayer Stacking Shifts at Anti-Phase Grain Boundaries in Overlapping MoS2 Secondary Layers. Nanoscale 2018, 10 (35), 16692–16702. https://doi.org/10.1039/c8nr04486d.

24   Chen, L.; Liu, B.; Ge, M.; Ma, Y.; Abbas, A. N.; Zhou, C. Step-Edge-Guided Nucleation and Growth of Aligned WSe2 on Sapphire via a Layer-over-Layer Growth Mode. ACS Nano 2015, 9 (8), 8368–8375. https://doi.org/10.1021/acsnano.5b03043.

25   Chubarov, M.; Choudhury, T. H.; Hickey, D. R.; Bachu, S.; Zhang, T.; Sebastian, A.; Bansal, A.; Zhu, H.; Trainor, N.; Das, S.; Terrones, M.; Alem, N.; Redwing, J. M. Wafer-Scale Epitaxial Growth of Unidirectional WS2Monolayers on Sapphire. ACS Nano 2021, 15 (2), 2532–2541. https://doi.org/10.1021/acsnano.0c06750.

26   Li,T., Guo, W., Ma, L., Li, W., Yu, Z., Han, Z., Gao, S., Liu, L., Fan, D., Wang, Z., Yang, Y., Lin, W., Luo, Z., Chen, X., Dai, N., Tu, X., Pan, D., Yao, Y., Wang, P., Nie, Y., Wang, J., Shi Y. and Wang, X., "Epitaxial growth of wafer-scale molybdenum disulfide semiconductor single crystals on sapphire," Nature Nanotechnology, 2021, 16, 1201-1207. https://doi.org/10.1038/s41565-021-00963-8.

27   Hwang, Y. and Shin, N. "Hydrogen assisted step-edge nucleation of MoSe2 monolayers on sapphire substrates," Nanoscale 2019, 11, 7701-7709. https://doi.org/10.1039/C8NR10315A.

28   Suenaga, K.; Ji, H. G.; Lin, Y.-C.; Vincent, T.; Maruyama, M.; Aji, A. S.; Shiratsuchi, Y.; Ding, D.; Kawahara, K.; Okada, S.; Panchal, V.; Kazakova, O.; Hibino, H.; Suenaga, K.; Ago, H. Surface-Mediated Aligned Growth of Monolayer MoS2 and In-Plane Heterostructures with Graphene on Sapphire. ACS Nano 2018, 12(10), 10032-10044. https://doi.org/10.1021/acsnano.8b04612.

29   Chubarov, M., Choudhury, T.H., Zhang X., Redwing, J.M., In-plane x-ray diffraction for characterization of monolayer and few-layer transition metal dichalcogenide films, Nanotechnol. 2018, 29, 055706. https://doi.org/10.1088/1361-6528/aaa1bd.

30   Tsuda, M., Watanabe, K., Kamiyama, S., Amano, H., Akasaki, I., Liu, R., Bell, A., Ponce, F.A., Mechanism of H2 pre-annealing on the growth of GaN on sapphire by MOVPE, Appl. Surf. Sci. 2003, 216, 585-589. https://doi.org/10.1016/S0169-4332(03)00449-5.

31   Reifsnyder Hickey, Danielle, et al. Illuminating invisible grain boundaries in coalesced single-orientation WS2 monolayer films. Nano Letters, 2021, 21 (15) 6487-6495. https://doi.org/10.1021/acs.nanolett.1c01517.

32   Huang, Pinshane Y., et al. Grains and grain boundaries in single-layer graphene atomic patchwork quilts. Nature 2011, 469, 389-392. https://doi.org/10.1038/nature09718

33   Zeng, H., Dai, J., Yao, W., Xiao, D. & Cui, X. Valley polarization in MoS2 monolayers by optical pumping. Nature Nanotechnology 2012, 7, 490-493. https://doi.org/10.1038/nnano.2012.95

34   Kim, J. et al. Ultrafast generation of pseudo-magnetic field for valley excitons in WSe2 monolayers. Science 2014, 346, 1205-1208. https://doi.org/10.1126/science.12581.

35   Yan, T., Qiao, X., Tan, P. & Zhang, X. Valley depolarization in monolayer WSe2. Scientific Reports 2015, 5, 15625. https://doi.org/10.1038/srep15625.

36   Zhu, B., Zeng, H., Dai, J., Gong, Z. & Cui, X. Anomalously robust valley polarization and valley coherence in bilayer WS2. Proceedings of the National Academy of Sciences 2014, 111, 11606. https://doi.org/10.1073/pnas.140696011.

37   Wang, J. et al. Dual-coupling-guided epitaxial growth of wafer-scale single-crystal WS2 monolayer on vicinal a-plane sapphire. Nature Nanotechnology 2022, 17, 33-38. https://doi.org/10.1038/s41565-021-01004-0.

Methods

MOCVD growth of WSe$_2$

The WSe$_2$ films were grown by MOCVD using two systems that are part of the 2D Crystal Consortium MIP facility at Penn State (http://www.mri.psu.edu/2d-crystal-consortium/user-facilities). The first system includes a cold-wall, horizontal reactor with inductive heating (MOCVD1) and the second is a multi-module system that includes a cold-wall vertical reactor with resistive heating (MOCVD2). In both systems, tungsten hexacarbonyl (W(CO)$_6$) and hydrogen selenide (H$_2$Se) were used as the metal and chalcogen precursors, respectively, with hydrogen (H$_2$) as the carrier gas. W(CO)$_6$ was kept in a stainless-steel bubbler held at a constant temperature (10-20 °C) and pressure (760 Torr), and H$_2$ gas was passed

through it to transport the precursor vapor to the reactor. Two-inch epi-ready c-plane sapphire ((0001)a-Al_2O_3) wafers with nominal miscut of 0.2° toward the m-axis were used as substrates for the growth without additional pre-treatment. The reactor pressure was kept constant at 200 Torr in MOCVD1 and was varied from 50-700 Torr in MOCVD2. For the growth of WSe_2, a modified three-step process (nucleation, ripening, lateral growth) was employed as illustrated in Figure S3.[1,2] Additional information on the growth conditions and recipes used for the WSe_2 growth are included in supplemental information.

Layer transfer process

The WSe_2 films were transferred from sapphire for TEM, Raman and photoluminescence (PL) spectroscopy. The typical transfer procedure involves coating an as-grown sample with poly(methyl methacrylate) (PMMA) using a spin-coater in two steps: 500 rpm for 15 s followed by 4500 rpm for 45 s. After curing PMMA at room temperature overnight, the sample edges are mechanically scratched to obtain open sapphire areas which will serve as starting points for the delamination process. The sample is then immersed into 1 M NaOH solution in de-ionized (DI) water and held at 90 °C for 10–15 min. At this point, a few mm at the periphery of the 2-inch WSe_2/PMMA films starts detaching from the sapphire substrate due to the combined effect of NaOH intercalation at the WSe_2/sapphire interface and sapphire surface etching. The sample is transferred to the top of DI water bath (at room temperature) where the delamination front rapidly (i.e. within a few tens of seconds) propagates through the entire WSe_2/PMMA film which peels off and stays afloat. This process is mostly aided by hydrophilic character of PMMA and the buoyancy of the WSe_2/PMMA film edges. The assembly is then transferred to a fresh DI water bath for 10 min for rinsing. This step is then repeated three more times to ensure the complete removal of residual NaOH from the previous step. The assembly is then fished out using a 3 mm diameter Cu Quantifoil TEM grid or 3-inch SiO_2/Si. After overnight drying at room temperature, the PMMA/WSe_2 film/target substrate assembly is heated at 50 °C for 10 min and at 70 °C for 10 more minutes. In the case of TEM, transfer is done so that the Quantifoil side touches the WSe_2 film. A fresh drop of PMMA is deposited onto the sample to gently soften the PMMA and improve the contact between WSe_2 film and the TEM grid. After about 30 min, the sample is placed into an acetone bath for the removal of PMMA film. The sample is then transferred into an alcohol (methanol or isopropanol) bath to remove acetone residue. The same procedure is followed for the transfer of the films to the other substrates.

First principles calculations

All first principles calculations on structural relaxation were conducted by the Vienna Ab Initio Package[3,4,5] using the generalized gradient approximation (GGA), Perdew–Burke–Ernzerhof (PBE)[6,7] exchange-correlation functional and the projector augmented wave method (PAW) pseudopotentials.[8,9] Plane-wave expansions were truncated at an energy cut-off of 400 eV with an electronic loop threshold of 0.1 meV. All structural relaxations were performed using dipole corrections to the total energy and to the electrostatic potential in the out-of-plane direction, until the remaining forces were within 0.01 eVÅ^{-1}. Gaussian smearing was used with a broadening of 0.05 eV, and van der Waals

interactions were treated using the semiempirical correction of Grimme (zero damping DFT-D3). Brillouin zone samplings were performed within a Γ-centered Monkhorst–Pack scheme on grids with k-point densities equivalent to that of a 20×20×1 grid for a 1×1 c-plane Al_2O_3 unit cell. A vacuum layer of 20 Å was inserted normal to the surface to minimize spurious interactions of periodic repetitions.

Material characterization

A Bruker Icon atomic force microscope (AFM) was used to study the surface morphology, domain size, coverage and thickness of the deposited layers. Scanasyst air probe AFM tips with a nominal tip radius of ~2 nm and spring constant of 0.4 N/m were employed for the measurements, and images were collected using peak-force tapping mode. To measure the thickness of the deposited films, samples were lightly scratched using a blunt tweezer to remove a portion of the weakly bonded WSe_2 film without damaging or scratching the sapphire surface. A Zeiss Merlin electron microscope was used for acquiring the scanning electron micrographs. An accelerating voltage of 3 kV and a working distance of 3 mm was used with the in-lens detector to capture the images. Room temperature Raman and photoluminescence were carried out using a Witec Apyron confocal microscope placed inside a MBraun glovebox to minimize oxygen (<1ppm) and moisture (<1ppm) influence. The laser has an excitation wavelength of 532 nm and the power remained under 4mW.

SHG measurements

Second harmonic generation (SHG) measurements were conducted using a 40 fs Ti:Sapphire laser (Micra, Coherent) at 800 nm and 80 MHz repetition rate. The laser beam was passed through a half-wave plate mounted in a rotation stage and was directed into an upright microscope (Olympus) and focused onto a sample surface using a 100x microscope objective (Numerical Aperture: NA=0.9) to a ~1 mm spot. The laser energy at the sample surface was ~ 0.1 mW. The SHG light was collected in backscattering configuration using the same objective and was directed to a monochromator (Spectra Pro 2300i, f = 0.3 m, Acton) that was coupled to the microscope and equipped with a 150 grooves/mm grating and a CCD camera (Pixis 256BR, Princeton Instruments). Before entering the monochromator, the SHG light was passed through a short-pass cut-off filter (650 nm) and a polarizer to filter out the fundamental excitation light at 800 nm and to select the SHG polarization parallel to that of the excitation light. The SHG mapping was conducted by moving a computer controlled motorized XY stage with 0.2 mm steps and acquiring an SHG spectrum at each step with the acquisition time of 0.5 s. To plot the maps, the SHG spectra at each step were integrated from 380 nm to 450 nm.

TEM characterization

Dark-field transmission electron microscopy (DFTEM) imaging was performed using a Thermo Fisher Talos F200X microscope operated at 80 kV. An array of 5x5 DFTEM images were stitched using the GIMP 2 image processing software to make a composite DFTEM map.[2] Briefly, the 25 DFTEM images are loaded into the software and the intensity of each image is adjusted to match with the neighboring images. At the end, all the Quantifoil regions have a similar intensity and all the freestanding monolayer

areas over the Quantifoil holes have a similar intensity. Consequently, the intensity in the bilayer areas will be higher than that of monolayer areas. Finally, the composite image is cropped to a size of 5 μm ´ 5 μm. Atomic resolution annual dark field-scanning TEM (ADF-STEM) images were obtained using Thermo Fisher Titan[3] G2 60-300 microscope operated at 80 kV. Other acquisition parameters used were 30 mrad semi convergence angle, 50 pA screen current and 42-244 mrad ADF detector collection angle range. A 2-pixel gaussian blur was applied to the ADF-STEM image shown in Figure S23d.

Cross-sectional TEM samples were prepared using a FEI Helios 660 focused ion beam (FIB) system. A thick protective amorphous carbon layer was deposited over the region of interest then Ga+ ions (30kV then stepped down to 1kV to avoid ion beam damage to the sample surface) were used in the FIB to make the electron-beam transparent samples. High resolution scanning transmission electron microscopy (STEM) was performed at 300 kV on a dual spherical aberration-corrected FEI Titan G2 60-300 S/TEM. All the STEM images were collected by using a high angle annular dark field (HAADF) detector with a collection angle of 50-100 mrad.

Low-temperature and polarization-dependent PL measurement

The WSe_2 transferred on Si was cooled down to 77 K by liquid nitrogen in a Janis ST-500 cryostat before PL measurement. The measurement was performed on a home-built optical spectroscope. The incident 532 nm CW laser is passed through a linear polarizer and a quarter wave plate to generate the left-handed circular polarized light which is focused on the sample using a 50x objective with an NA of 0.4. The circular polarized PL signal was collected by the same quarter-wave plate and another linear polarizer, which was rotated to select the polarization of the PL signals. The laser power used was around 0.2 mW.

References

1. Zhang, X.; Choudhury, T. H.; Chubarov, M.; Xiang, Y.; Jariwala, B.; Zhang, F.; Alem, N.; Wang, G. C.; Robinson, J. A.; Redwing, J. M. Diffusion-Controlled Epitaxy of Large Area Coalesced WSe2 Monolayers on Sapphire. *Nano Lett.* **2018**, 18 (2), 1049−1056.

2. Chubarov, M.; Choudhury, T. H.; Hickey, D. R.; Bachu, S.; Zhang, T.; Sebastian, A.; Bansal, A.; Zhu, H.; Trainor, N.; Das, S.; Terrones, M.; Alem, N.; Redwing, J. M. Wafer-Scale Epitaxial Growth of Unidirectional WS2 Monolayers on Sapphire. *ACS Nano* **2021**, 15 (2), 2532−2541.

3. Kresse, G. & Furthmüller, J. Efficiency of ab-initio total energy calculations for metals and semiconductors using a plane-wave basis set. *Comput. Mater. Sci.* **1996**, 6, 15−50. https://doi.org/10.1016/0927-0256(96)00008-0.

4. Kresse, G. & Furthmüller, J. Efficient iterative schemes for ab initio total-energy calculations using a plane-wave basis set. *Phys. Rev. B* **1996**, 54, 11169−11186. https://doi.org/10.1103/PhysRevB.54.11169.

5. Kresse, G. & Hafner, J. Ab initio molecular dynamics for liquid metals. *Phys. Rev. B* **1993**, 47, 558–561. https://doi.org/10.1103/PhysRevB.47.558.

6. Perdew, J. P., Burke, K. & Ernzerhof, M. Generalized Gradient Approximation Made Simple. *Phys. Rev. Lett.* **1996**, 77, 3865–3868. https://doi.org/10.1103/PhysRevLett.77.3865.

7. Perdew, J. P., Burke, K. & Ernzerhof, M. Generalized Gradient Approximation Made Simple [Phys. Rev. Lett. 77, 3865 (1996)]. *Phys. Rev. Lett.* **1997**, 78, 1396–1396. https://doi.org/10.1103/PhysRevLett.78.1396.

8. Kresse, G. & Joubert, D. From ultrasoft pseudopotentials to the projector augmented-wave method. *Phys. Rev. B* **1999**, 59, 1758–1775. https://doi.org/10.1103/PhysRevB.59.1758.

9. Kresse, G. & Hafner, J. Norm-conserving and ultrasoft pseudopotentials for first-row and transition elements. *J. Phys. Condens. Matter* **1994**, 6, 8245–825. https://doi.org/10.1088/0953-8984/6/40/015.
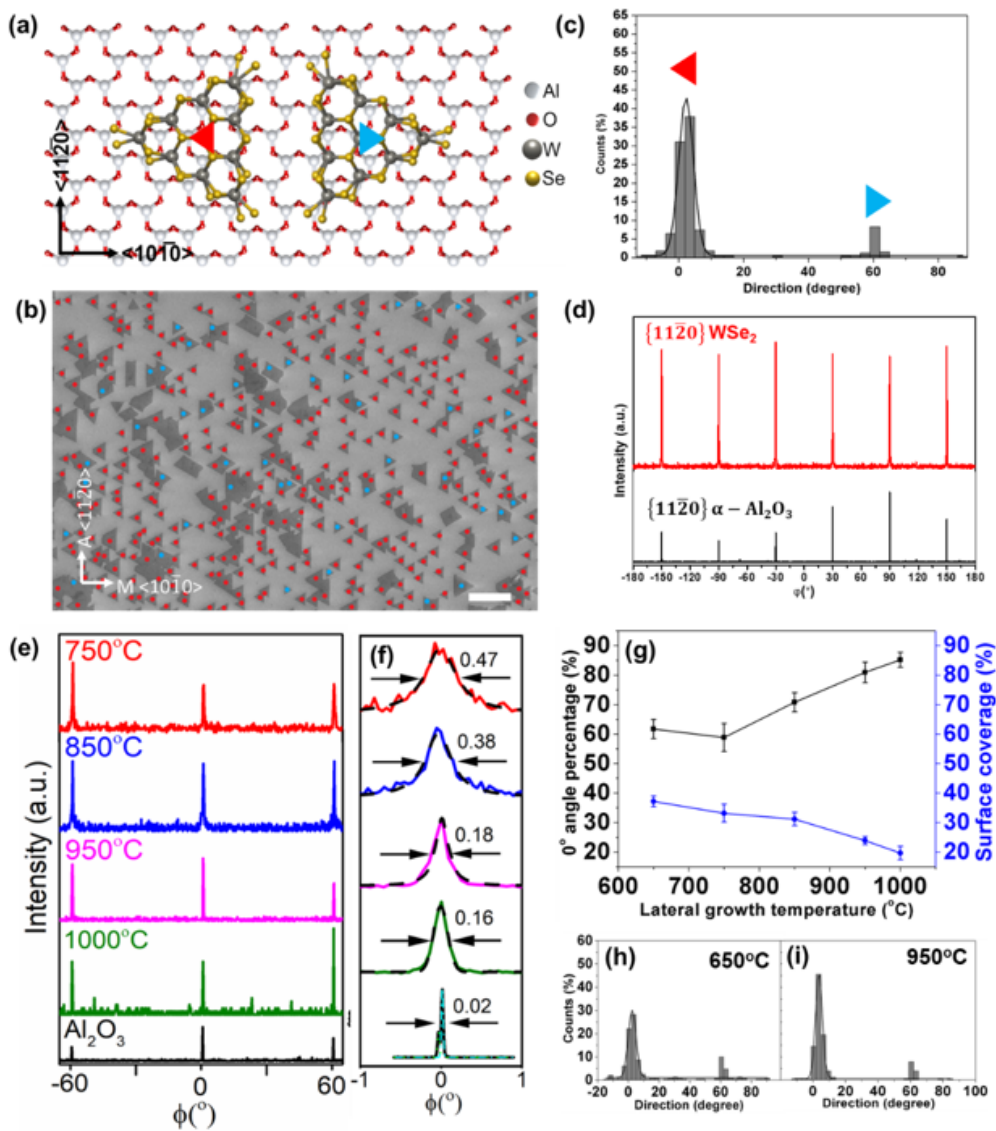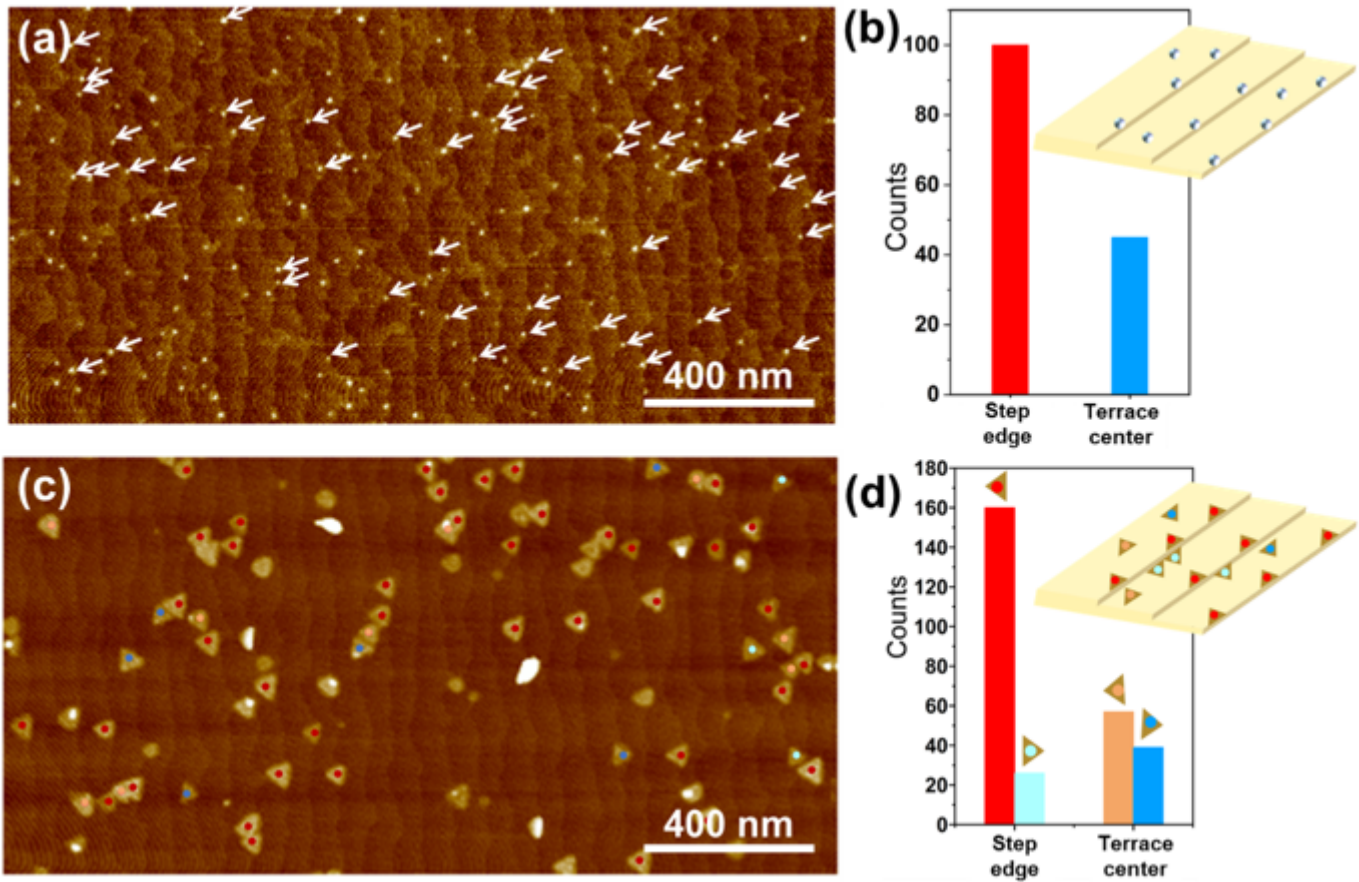
Figures

Figure 1. (a) Schematic illustration and (b) SEM image of WSe$_2$ domains showing a preferred orientation of 0° (red) and 60° (blue) oriented WSe$_2$. Scale bar in (b) is 1 μm. (c) Orientation histogram of the isolated WSe$_2$ domains in (b). (d) In-plane XRD φ-scans of {11$\bar{2}$0} planes of WSe$_2$ and α-Al$_2$O$_3$ confirming the six-fold [11$\bar{2}$0]WSe$_{2(0001)}$ // [11$\bar{2}$0]α-Al$_2$O$_{3(0001)}$ epitaxial relationship. (e) In-plane XRD φ-scans of {10$\bar{1}$0} planes of WSe$_2$ as a function of lateral growth temperature. (f) The FWHM of the WSe$_2$ φ-scan peak decreases with increasing temperature indicating a reduction in in-plane rotational misorientation. (g) Percentage of 0° oriented WSe$_2$ domains and surface coverage as a function of growth temperature obtained from atomic force microscopy (AFM) images and orientation histograms (h-i and Fig. S5).
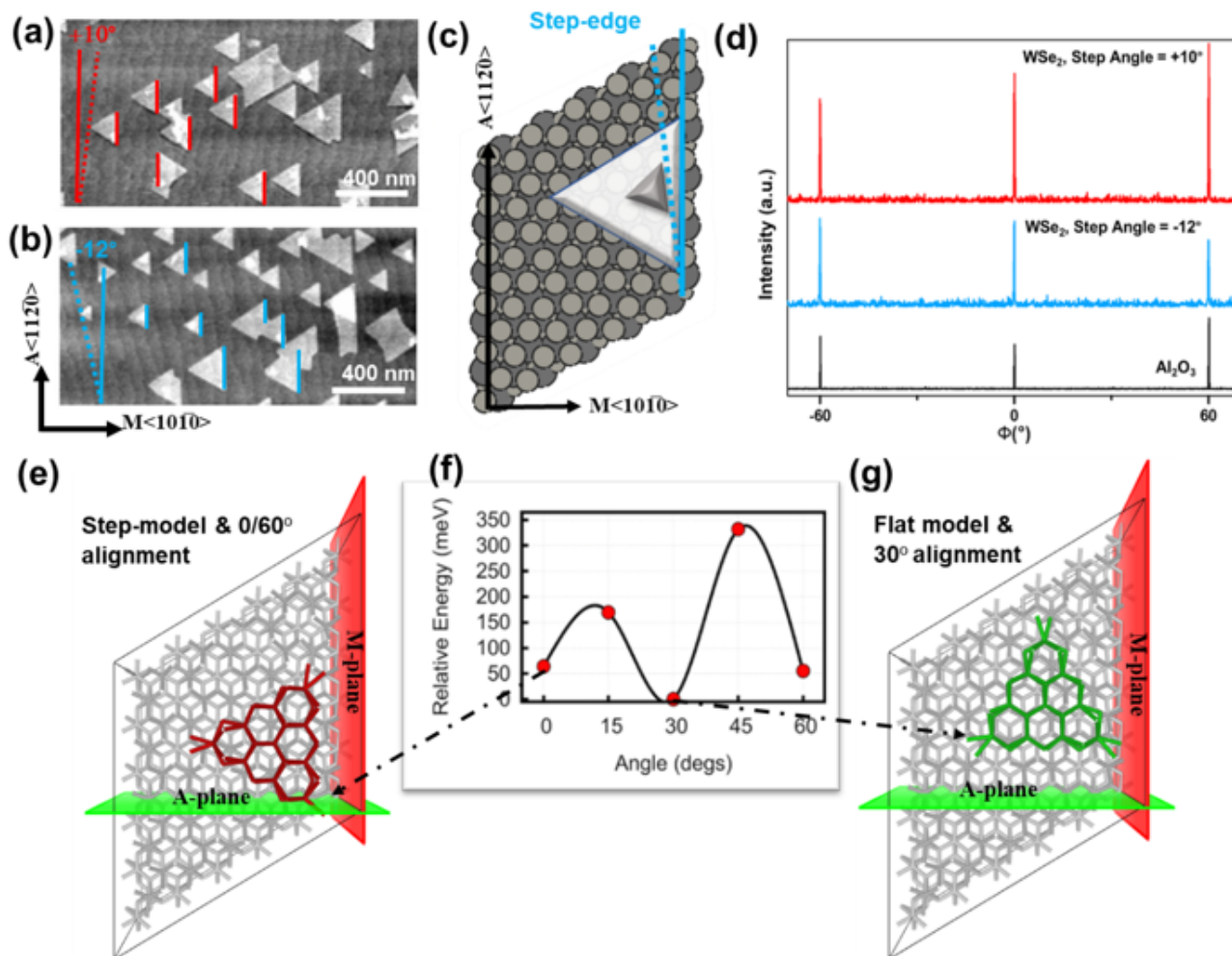
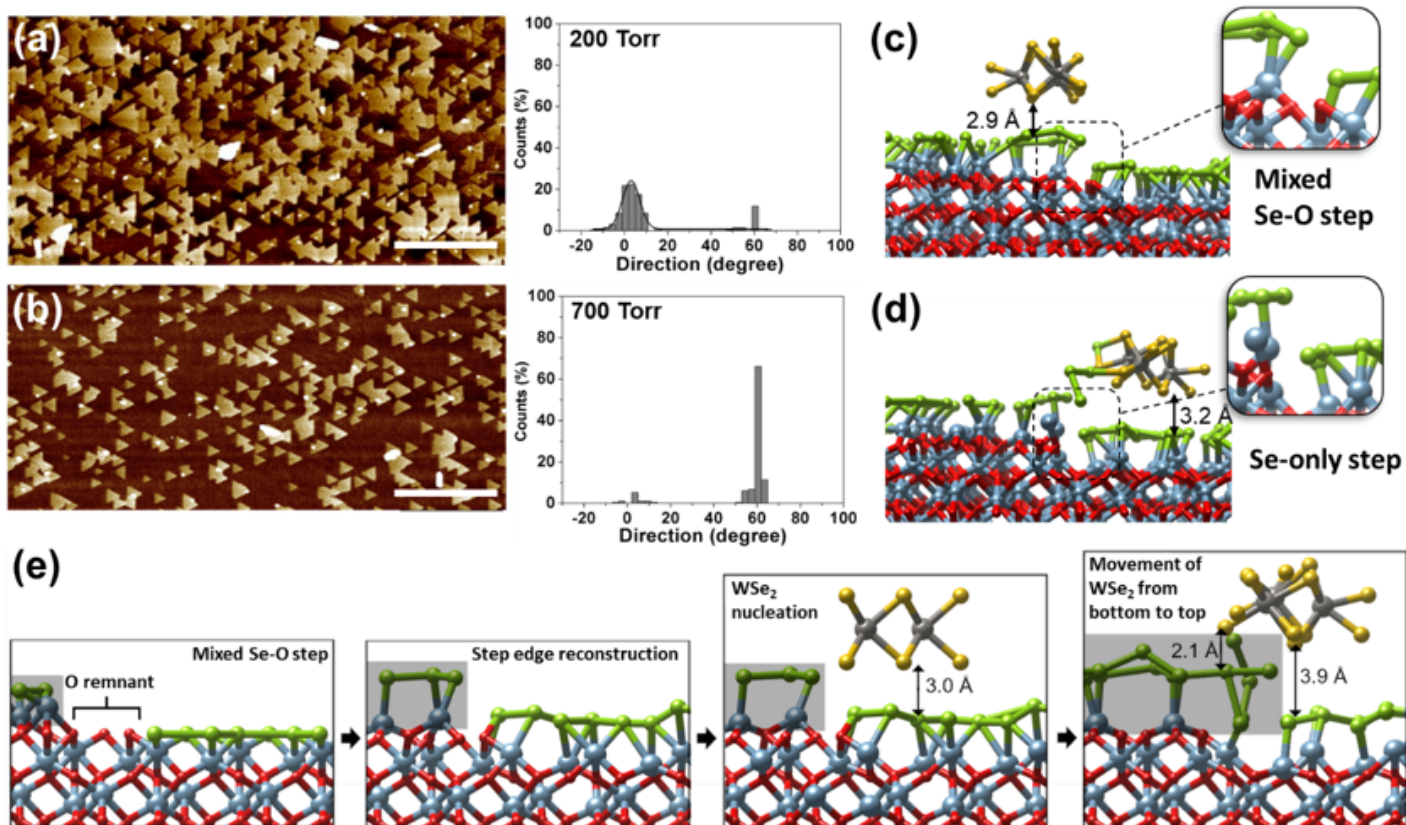# Figure 1

See above image for figure legend.

Figure 2

(a) AFM image showing WSe$_x$ nuclei on the sapphire substrate after nucleation and ripening. The white arrows highlight the nuclei localized at the step edges. (b) Position distribution and schematic of nuclei at step edges (red) and terrace centers (blue). (c) AFM image of WSe$_2$ domains after 5 min lateral growth. The dots on the domains are color coded according to their location and orientation as shown in (d).

Figure 3. Competition between the step edge and underlying sapphire symmetry – (a, b) Two samples where the steps are oriented at +10° and -12° relative to the A-axis of the sapphire yet the zig-zag edge of the WSe_2 domains remains parallel to the $A<11\bar{2}0>$ axis as shown schematically in (c). (d) In-plane XRD ϕ-scans of $\{11\bar{2}0\}$ planes confirming that the WSe_2 remains epitaxially aligned to the Al_2O_3. (e, g) WSe_2 alignment on sapphire in the presence/absence of step edges and (f) energetics of WSe_2 on a flat c-plane sapphire as a function of orientation angle.
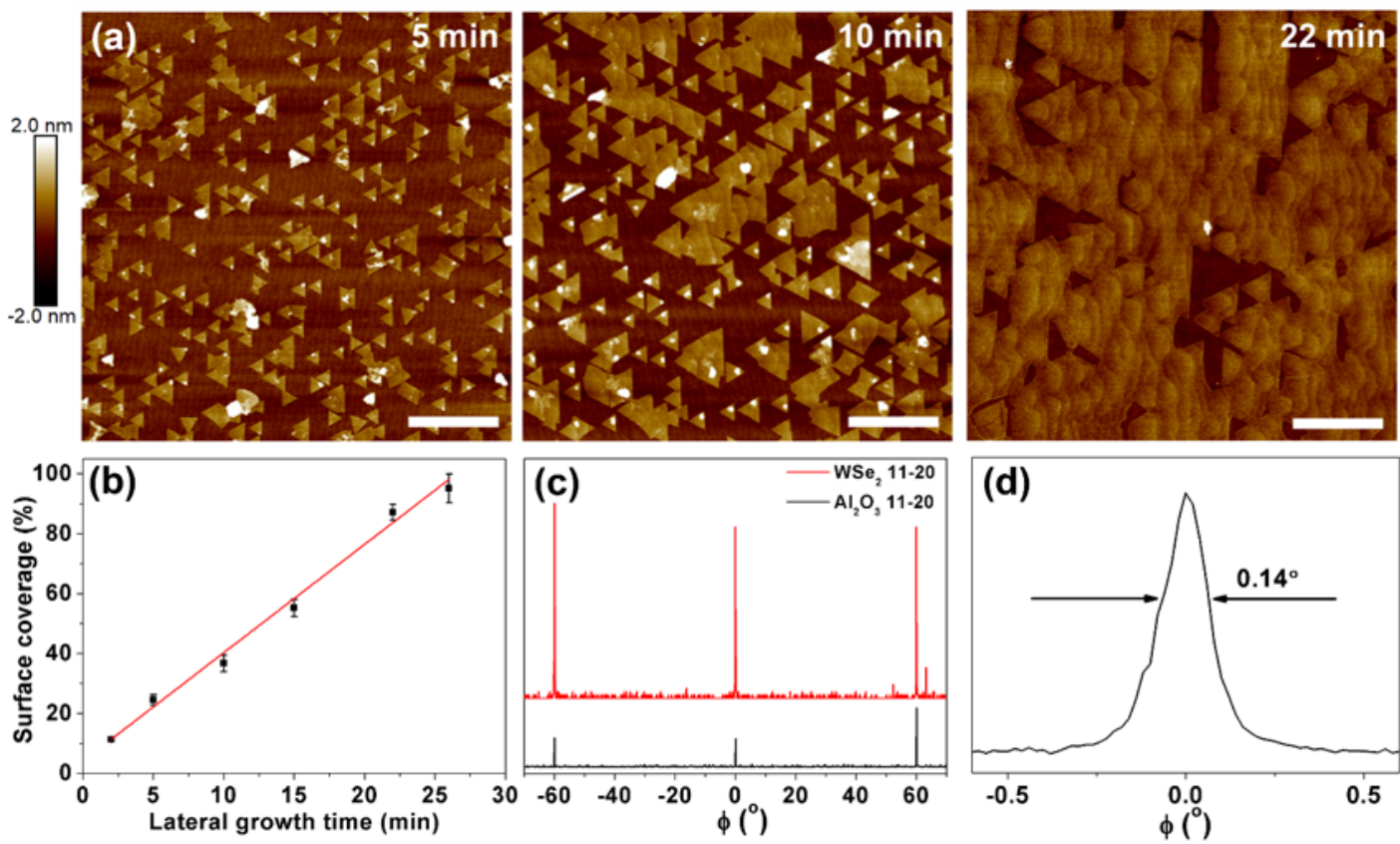
Figure 3

See above image for figure legend.

Figure 4

AFM image and histograms of WSe_2 domains grown on c-plane sapphire at (a) 200 Torr and (b) 700 Torr showing preferred orientations of 0° and 60°, respectively. Optimized configuration of (c) a mixed Se-O and (d) single Se-atom stepped sapphire with oxidized region on the bottom terrace next to the step edge. (e) Step edge reconstruction on mixed Se-O stepped sapphire. During the relaxation, the existence of O-remnant leads to the step edge reconstruction (highlighted with a gray background, then the movement of WSe_2 from the bottom to the top terrace as shown also in Fig. S11 and Movies S1-S4.

Figure 5. (a) AFM images and (b) percentage of surface coverage of WSe$_2$ domains as a function of lateral growth time showing the coalescence of domains. (b) In-plane XRD ϕ-scans showing alignment of $[11\bar{2}0]$ planes of WSe$_2$ and Al$_2$O$_3$. (d) FWHM of ϕ-scan peak of WSe$_2$.

Figure 5

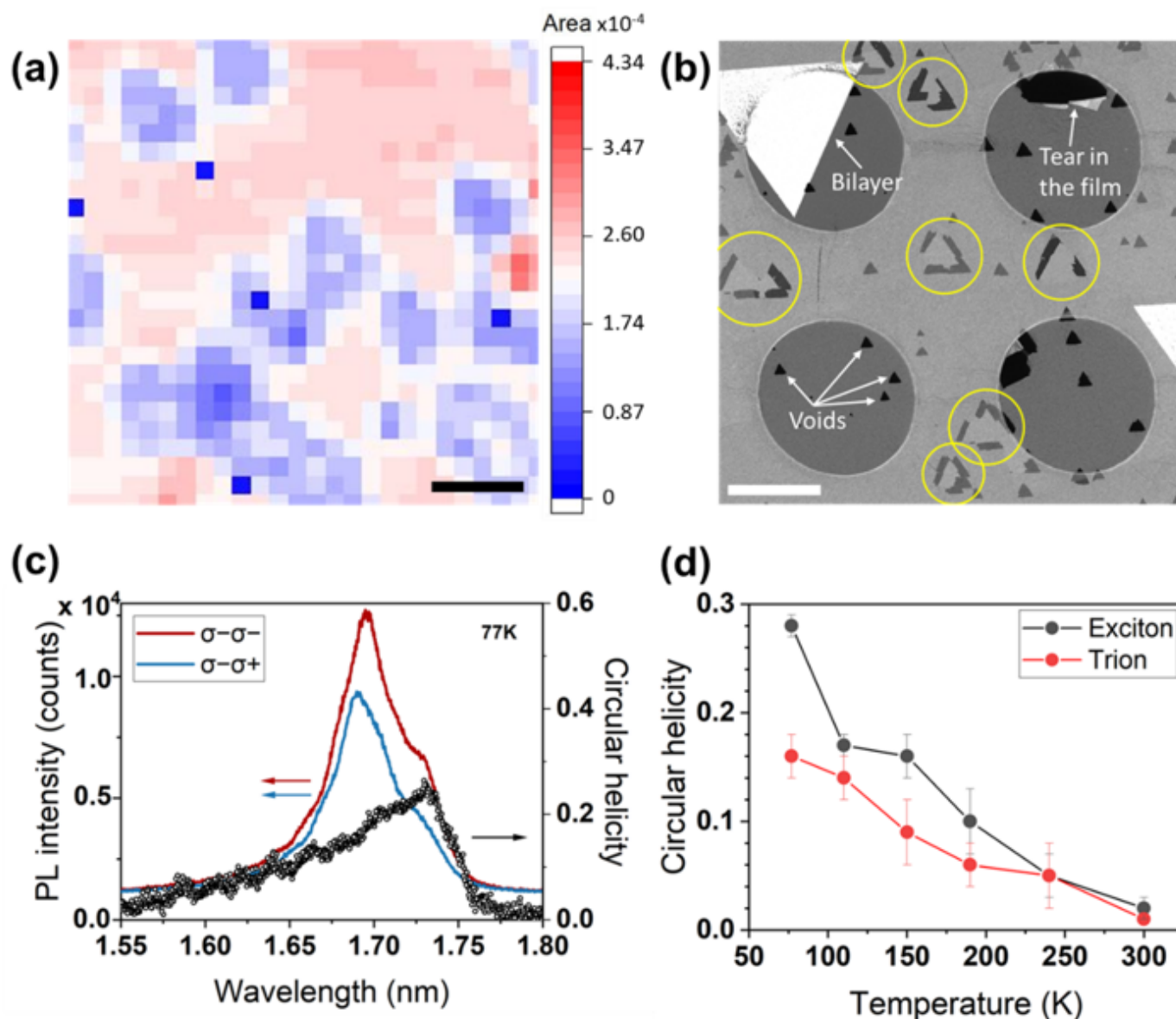See above image for figure legend.

Figure 6

(a) SHG map of WSe_2 on c-plane sapphire; (b) Composite DF-TEM map of WSe_2 transferred on a TEM grid; (c) Polarization-resolved PL spectra and circular helicity of transferred WSe_2 at 77K. The incident laser was left-handed circular polarized while both left-handed and right-handed circular polarizations were collected, denoted as σ–σ– and σ–σ+. (d) Circular helicities at the energies of the exciton and trion as a function of temperature.

Supplementary Files

This is a list of supplementary files associated with this preprint. Click to download.

- MovieS1mixedstepbottomterracetriangle.mp4

- MovieS2mixedsteptopterracetriangle.mp4
- MovieS3singlestepbottomterracetriangle.mp4
- MovieS4singlesteptopterracetriangle.mp4
- MovieS5mixedstepbottomterraceribbon.mp4
- MovieS6mixedsteptopterraceribbon.mp4
- MovieS7singlestepbottomterraceribbon.mp4
- MovieS8singlesteptopterraceribbon.mp4
- 20221016AlignedWSe2Draft20SupplementaryInformationFINAL.docx